

Study of structure and lattice dynamics of the $\text{Sr}_2\text{CuO}_2\text{Cl}_2(001)$ surface by helium-atom scattering

M. Farzaneh, XF. Liu, and M. El-Batanouny

Department of Physics, Boston University, 590 Commonwealth Avenue, Boston Massachusetts 02215

F.C. Chou

Center for Materials Science and Engineering, Massachusetts Institute of Technology, Cambridge, Massachusetts 02139

Structure and lattice dynamics of the (001) surface of $\text{Sr}_2\text{CuO}_2\text{Cl}_2$ have been studied by helium atom scattering (HAS). Analysis of diffraction patterns obtained by elastic HAS revealed a surface periodicity consistent with bulk termination, and confirms that the surface is non-polar and stable which favors a SrCl surface termination. Bulk and surface lattice dynamical calculations based on the shell-model were carried out to characterize the experimental phonon dispersions obtained by inelastic HAS. No experimental surface mode was observed above 200 cm^{-1} . Comparison between the experimental data and theoretical results for two different slabs with SrCl and CuO_2 terminations showed that the experimental data conforms exclusively with the SrCl surface modes.

PACS numbers:

I. INTRODUCTION

Surface lattice dynamics of metals, semiconductors, simple insulators and layered structures¹ have been studied extensively. However, high temperature superconductors (HTSC), their parent compounds and related lamellar cuprates are more complex in structure and dynamics and the study of their surface dynamical properties has been limited to only a few cases^{2,3}. Because of the established relation between phonons and superconductivity in conventional superconductors, bulk phonons of the HTSC and their parent compounds received considerable attention in the early years following their discovery. Optical spectroscopies (infrared (IR) and Raman)^{4,5,6,7,8,9} and neutron scattering experiments^{10,11,12} were used to study the lattice dynamics of these compounds. Although it is believed that spin interactions play an important role in the superconducting properties of HTSC cuprates, the role of the electron-phonon coupling still remains a puzzle. For example, the isotope effect in the optimally doped cuprates is very small¹³, but away from optimal doping a large isotope effect has been observed¹⁴. In addition, the highest longitudinal optical (LO) phonon branch softens and shows line-width broadening when the parent compounds of several HTSC, such as $\text{La}_{2-x}\text{Sr}_x\text{CuO}_4$ ^{15,16} and $\text{YBa}_2\text{Cu}_3\text{O}_{6+y}$ ¹⁷, are hole-doped to a superconducting state. Furthermore, in recent angle resolved photoemission spectroscopy (ARPES) experiments on several HTSC materials, an abrupt change of electron velocity at 50-80 meV has been observed¹⁸ which is interpreted to be caused by the coupling of electrons to the LO phonon modes in the same energy range. Whether these effects suggest that electron-phonon coupling in HTSC can drive electron-pairing or it is just a secondary mechanism that occurs naturally in an interacting system without affecting the superconducting pairing mechanism is still open to discussion and interpretation¹⁹. Therefore the role of

phonons in HTSC is still not completely understood and electron-phonon coupling can still effect the superconducting state. For this reason lattice dynamical studies of these compounds and related cuprates are still important.

In this paper we report on the study of the structure and dynamics of the (001) surface of $\text{Sr}_2\text{CuO}_2\text{Cl}_2$. In the bulk, this compound is a layered perovskite with the body centered tetragonal structure of K_2NiF_4 type and space group $I4/mmm(D_{4h}^{17})$ ²⁰. It consists of CuO_2 sheets separated by double layers of SrCl. Neutron diffraction studies²⁰ show that the lattice parameters for $\text{Sr}_2\text{CuO}_2\text{Cl}_2$ at room temperature are $a = 3.9716 \text{ \AA}$ and $c = 15.6126 \text{ \AA}$. The crystal structure of $\text{Sr}_2\text{CuO}_2\text{Cl}_2$ is shown in Figure 1. $\text{Sr}_2\text{CuO}_2\text{Cl}_2$ is also isostructural to the high-temperature phase of La_2CuO_4 , but with the out of plane oxygen ions at the apices of the CuO_6 octahedra replaced by Cl and the La by Sr.

However two clear differences between $\text{Sr}_2\text{CuO}_2\text{Cl}_2$ and La_2CuO_4 stand out: unlike La_2CuO_4 , which undergoes a structural phase transition from tetragonal to orthorhombic symmetry at about 530 K²¹ involving rotations of the CuO_6 octahedra, no evidence of a structural distortion has been observed in $\text{Sr}_2\text{CuO}_2\text{Cl}_2$ down to 10 K^{20,22}. Also in contrast to La_2CuO_4 , which can be doped by substitution of La with a divalent ion like Sr^{+2} and shows a superconducting behavior below $T_c \sim 40\text{K}$, neither electron nor hole doping of $\text{Sr}_2\text{CuO}_2\text{Cl}_2$ has been possible²³, although the similarly structured $\text{Ca}_2\text{CuO}_2\text{Cl}_2$ can be doped successfully by Na with $T_c \sim 28 \text{ K}$ ²⁴ and very recently superconductivity at $T_c \sim 30 \text{ K}$ has been reported in apical oxygen doped $\text{Sr}_2\text{CuO}_{2+\delta}\text{Cl}_{2-y}$ ²⁵.

Neutron diffraction experiments^{22,26,27,28,29} have been used to explore the similarities and differences between the magnetic properties of $\text{Sr}_2\text{CuO}_2\text{Cl}_2$ and La_2CuO_4 and to understand the magnetic interactions in these two-dimensional (2D) spin-1/2 systems. In particular, it is shown that both $\text{Sr}_2\text{CuO}_2\text{Cl}_2$ and La_2CuO_4 are

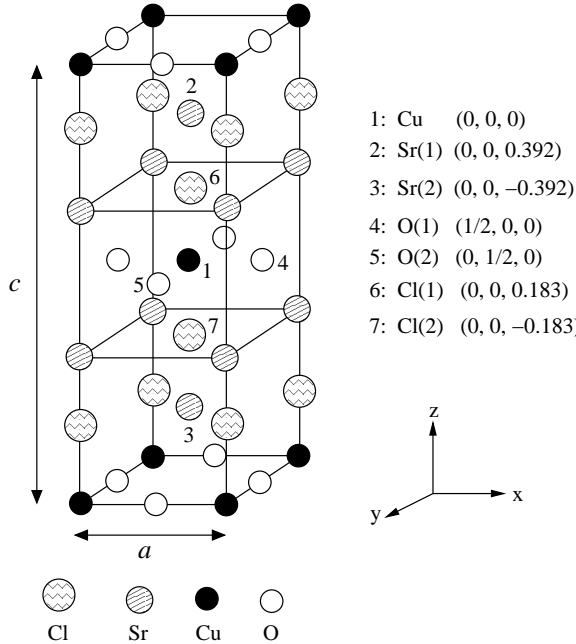


FIG. 1: Crystal structure and positions of the atoms in $\text{Sr}_2\text{CuO}_2\text{Cl}_2$. Atomic positions are taken from Ref. 20.

antiferromagnetic (AFM) insulators with Néel temperatures (T_N) of about 250 K and 300 K, respectively, and have similar intralayer exchange coupling J of about 130 meV; in the paramagnetic phase both are good examples of 2D square lattice quantum Heisenberg antiferromagnets (2DSLQHA)^{21,29}. The main difference between the magnetic properties of these two compounds is that the orthorhombic distortion in La_2CuO_4 allows for a Dzyaloshinsky-Moriya (DM) antisymmetric exchange interaction in the spin Hamiltonian which is absent in $\text{Sr}_2\text{CuO}_2\text{Cl}_2$ because of the stability of its tetragonal structure to the lowest temperatures measured²¹. The DM interaction in La_2CuO_4 leads to a weak ferromagnetic moment perpendicular to CuO_2 planes³⁰. However, the weak inter-layer coupling causes the moments of successive layers to order antiferromagnetically, so the weak ferromagnetism is hidden in the Néel state at zero field^{21,31}.

In light of the above discussions, and the fact that $\text{Sr}_2\text{CuO}_2\text{Cl}_2$ has the advantage that it can be easily cleaved, a study of the surface lattice dynamics of $\text{Sr}_2\text{CuO}_2\text{Cl}_2$ can not only provide information about the bulk phonons of this compound, which are currently limited to a few optical spectroscopy studies, but also provide insight as to the modifications effected at the surface to the vibrational modes of the bulk for La_2CuO_4 , where the bulk dynamics has already been studied but no surface phonon study exists.

II. EXPERIMENTAL PROCEDURE

The single crystalline samples of $\text{Sr}_2\text{CuO}_2\text{Cl}_2$ used in our experiments were grown at MIT crystal growth facility. The samples were plate like with the c -axis perpendicular to the sheets of the plate. They were cut to dimensions of about $7 \times 7 \times 0.5$ mm and mounted on a copper sample holder by silver conducting epoxy. A cleaving post was then attached to the sample surface, also by the epoxy. The prepared sample was mounted on a manipulator which accommodated xyz motions, as well as polar and azimuthal rotations. The *in situ* ultra-high vacuum (UHV) cleaving of the sample was implemented by the top-post method by knocking off the post on the surface. Immediately after cleaving, the quality of the long range ordering on the surface was checked by low energy electron diffraction (LEED). The LEED images were sharp spots and ordered in a square pattern, with no discernable satellites.

Elastic and inelastic He-atom scattering (HAS) techniques were used for measuring the structure and dynamics of the surface. Since about 1975, novel surface spectroscopic methods based on the interaction of thermal energy neutral helium atoms with solid surfaces have become possible due to the progress in combining high-resolution He beam production systems with UHV techniques. Because of their low kinetic energies (10 - 100 meV), inert He-atom beams probe the topmost layer of the surface in a non-destructive manner. In addition, momenta of thermal-energy He atoms are of the order of the surface phonon momenta, making HAS suitable for scanning the entire surface Brillouin zone. Therefore helium atom scattering is our method of choice for the study of the structure and vibrations of the surface.

A mono-energetic supersonic beam of thermal-energy neutral He atoms is generated by a nozzle-skimmer assembly and directed to the scattering chamber through various collimating slits. The energy of the He beam can be varied from $E_i = 25$ meV to $E_i = 65$ meV by changing the nozzle temperature from 110 K to 300 K. The temperature is controlled and measured by a diode sensor together with a temperature controller (Scientific Instruments, Model 9600-1). Polar rotation of the sample allows the variation of the He beam incident angle θ_i with respect to the surface normal. The scattered He beam is collected by an angle resolved detector mounted on a two-axis goniometer which allows the scattering angle θ_f to be varied independently. The detector is comprised of an electron gun and a multichannel plate (MCP) electron multiplier. The electron gun generates a well-collimated, monoenergetic electron beam crossing the He beam at right angles. The energy of the electron beam is tuned to excite the He atoms to their first excited metastable state (2^3S He^*) upon impact. Deexcitation of a He^* atom at the surface of the MCP leads to the ejection of an electron which generates an electron cascade that is then collected by the anode of the multiplier. By electronically pulsing the electron gun a gate function is created for

time-of-flight (TOF) measurements in the inelastic HAS mode. The details of the detection scheme are given in Ref 32. All the measurements are performed with the sample surface at room temperature.

By writing the He-atom wave vector as $\mathbf{k} = (\mathbf{K}, k_z)$, where \mathbf{K} is the component parallel to the surface, conservation of momentum and energy for in-plane He scattering can be expressed as

$$\Delta\mathbf{K} = k_f \sin \theta_f - k_i \sin \theta_i = \mathbf{G} + \mathbf{Q}, \quad (1)$$

and

$$\Delta E = \hbar\omega(\mathbf{Q}) = E_f - E_i = \frac{\hbar^2}{2m} (k_f^2 - k_i^2), \quad (2)$$

where subscripts i and f denote incident and scattered beams, respectively and $\Delta\mathbf{K}$ is the momentum transfer parallel to the surface. \mathbf{G} is a surface reciprocal lattice vector, \mathbf{Q} is the surface phonon wave vector and $\hbar\omega(\mathbf{Q})$ is the corresponding surface phonon energy. By eliminating k_f from the above equations one obtains the so-called *scan curve* relations which are the locus of all the allowed ΔE and $\Delta\mathbf{K}$ as dictated by the conservation relations:

$$\Delta E = E_i \left[\left(\frac{\sin \theta_i + \Delta K/k_i}{\sin \theta_f} \right)^2 - 1 \right]. \quad (3)$$

The intersections of these scan curves with the phonon dispersion curves define the kinematically allowed inelastic events for a fixed geometric arrangement. Thus, by systematically changing E_i , θ_i and θ_f the entire dispersion curves can be constructed.

III. RESULTS

A. Elastic He Scattering

Figure 2 shows two typical He diffraction patterns from the (001) surface of $\text{Sr}_2\text{CuO}_2\text{Cl}_2$ along $\langle 100 \rangle$ and $\langle 110 \rangle$ symmetry directions for $\theta_i = 40^\circ$ and 35° , respectively. The curves are shown as a function of the parallel momentum transfer $\Delta\mathbf{K}$. The surface periodicity is obtained from the positions of the diffraction peaks along each direction resulting from the Bragg relation

$$\Delta\mathbf{K} = n G_{\langle 100 \rangle}, \quad \text{or} \quad \Delta\mathbf{K} = n G_{\langle 110 \rangle}, \quad (4)$$

where integer n indicates the order of diffraction. From these and the position of Bragg peaks obtained from other diffraction patterns taken at various incident angles, the value of $a = 3.97 \text{ \AA}$ for the surface lattice parameter was obtained. This value is very close to the lattice parameter reported for the bulk²⁰. This, and the fact that no systematic satellite peaks in the diffraction patterns were observed, suggest a bulk like termination at the surface and indicates surface stability against reconstruction.

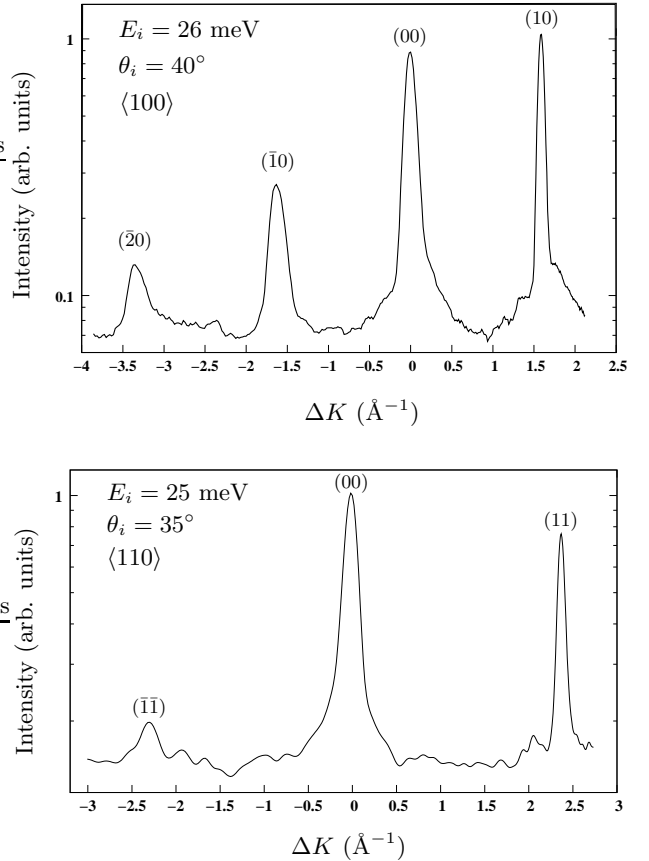


FIG. 2: Typical diffraction patterns along $\langle 100 \rangle$ and $\langle 110 \rangle$ azimuth directions for cleaved $\text{Sr}_2\text{CuO}_2\text{Cl}_2(001)$ surface. The intensity scale is logarithmic.

In general, cleaving the $\text{Sr}_2\text{CuO}_2\text{Cl}_2$ can result in two different surfaces with different compositions as shown in Figure 3. SrCl termination of the crystal results in a non-polar surface which, according to Tasker's classification of ionic surfaces³³, consists of a neutral repeat unit of $\text{SrCl} - \text{CuO}_2 - \text{SrCl}$, and is stable. However, termination at a CuO_2 layer, results in a repeat unit of $\text{CuO}_2 - \text{SrCl}$ which has a non-vanishing dipole moment perpendicular to the surface. Such a polar surface cannot be stable because of the divergence of the electrostatic energy contribution to the surface energy. Hence, such termination would be allowed only if the surface undergoes a reconstruction resulting in cancellation of the dipole moment perpendicular to the surface. The apparent surface stability against reconstruction on the (001) surface of $\text{Sr}_2\text{CuO}_2\text{Cl}_2$ suggests that the top-most layer is indeed SrCl and *not* CuO_2 . This is also supported by previous LEED and x-ray photoemission spectroscopy studies of the $\text{Sr}_2\text{CuO}_2\text{Cl}_2(001)$ surface^{34,35,36} which suggest that SrCl is the top-most layer.

From the intensity analysis of the diffraction peaks, one can obtain the surface corrugation function. A two dimensional surface corrugation consistent with the $4mm$

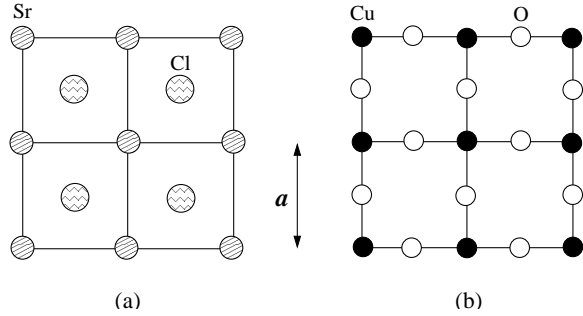


FIG. 3: Schematic illustration of two different possible (001) surfaces created by cleaving $\text{Sr}_2\text{CuO}_2\text{Cl}_2$: (a) SrCl and (b) CuO_2 .

symmetry of the surface was chosen as

$$\begin{aligned} \zeta(x, y) = & \zeta_1 \left[\cos\left(\frac{2\pi x}{a}\right) + \cos\left(\frac{2\pi y}{a}\right) \right] \\ & + \zeta_2 \left[\cos\left(\frac{2\pi(x+y)}{a}\right) + \cos\left(\frac{2\pi(x-y)}{a}\right) \right], \end{aligned} \quad (5)$$

where ζ_1 and ζ_2 denote the corrugation amplitudes and are taken as model parameters. Values of $\zeta_1 = 0.01 \text{ \AA}$ and $\zeta_2 = 0.15 \text{ \AA}$ were obtained by fitting Bragg peak intensities calculated within the framework of the eikonal approximation³⁷ and using an attractive potential well depth of $D = 10 \text{ meV}$ to the experimental intensities. To back up this calculation we also obtained the corrugation amplitudes by calculating the surface charge density $\rho(x, y, z)$, since the corrugation function is the locus of the classical turning points for He atoms at a fixed surface charge density contour. $\rho(x, y, z)$ was constructed as a superposition of the individual atomic charge densities at a SrCl surface. The atomic charge densities for Sr and Cl were derived using the atomic wave functions of Herman and Skillman³⁸. The values of ζ_1 and ζ_2 calculated at a constant contour of $\rho(x, y, z)$ at a turning point of 2.7 \AA above the surface were 0.01 \AA and 0.147 \AA , which are very close to the values obtained by the eikonal approximation.

B. Surface Phonons

Surface phonon energies were measured along the $\bar{\Delta}$ and $\bar{\Sigma}$ directions of the surface Brillouin zone (SBZ), shown in Figure 4. Two typical TOF spectra showing diffusive elastic, as well as inelastic peaks are shown in Figure 5. The data were collected using beam energies in the range of $25 - 65 \text{ meV}$. The high energy He beam ($E_i \sim 65 \text{ meV}$) was used to probe the high-frequency surface phonon modes. The energy resolution for the lowest energy beam was about 3 meV . Phonon energies and momenta were calculated from the TOF peak positions, after a Gaussian fit to the peaks, using Eqs.(1)

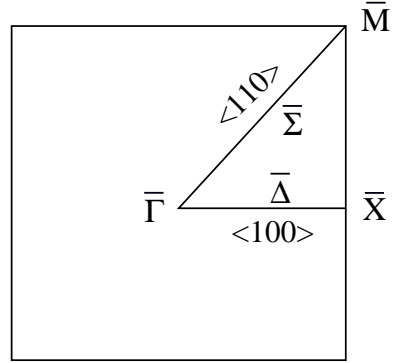


FIG. 4: Surface Brillouin zone and the high symmetry directions.

and (2). To characterize the ensuing phonon dispersion points lattice dynamical analysis for the bulk and surface (slab calculation) were carried out as outlined in the next section.

IV. LATTICE DYNAMICAL ANALYSIS

A. Static Equilibrium and Bulk Lattice Dynamics

In lattice dynamical studies of the cuprates and HTSC parent compounds, the construction of a dynamical matrix based on pair potentials rather than mere force constants is far more advantageous in the sense that the underlying physics is transparent and many of the potential parameters for similar pair interactions can be transferred from one compound to another^{39,40}. This is specially useful for compounds like $\text{Sr}_2\text{CuO}_2\text{Cl}_2$ for which experimental phonon frequencies are limited to four infrared (IR)-active phonon modes at the center of the Brillouin zone (BZ)^{41,42}, and no neutron scattering data for phonons are available. However, experimental and theoretical studies of bulk lattice dynamics of the isostructural La_2CuO_4 are extensive and contain detailed information about relevant model potentials^{4,5,8,11,12,43}. Therefore, for some of the pair interactions which are similar in both compounds (such as Cu-O and O-O), the existing potential parameters for La_2CuO_4 can be transferred to $\text{Sr}_2\text{CuO}_2\text{Cl}_2$. In $\text{Sr}_2\text{CuO}_2\text{Cl}_2$, with seven atoms per primitive cell, more model parameters can be determined by fulfilling the static equilibrium conditions which state that the forces on the particles in their equilibrium positions should vanish. This treatment also ensures the consistency of the static and dynamical properties of the crystal. It should be noted, however, that satisfying static equilibrium conditions, does not guarantee any dynamical stability, namely ensuring the reality of the phonon frequencies throughout the BZ.

The model used for both static equilibrium calculations and lattice dynamics (shell-model) of bulk $\text{Sr}_2\text{CuO}_2\text{Cl}_2$, incorporates two-body central potentials,

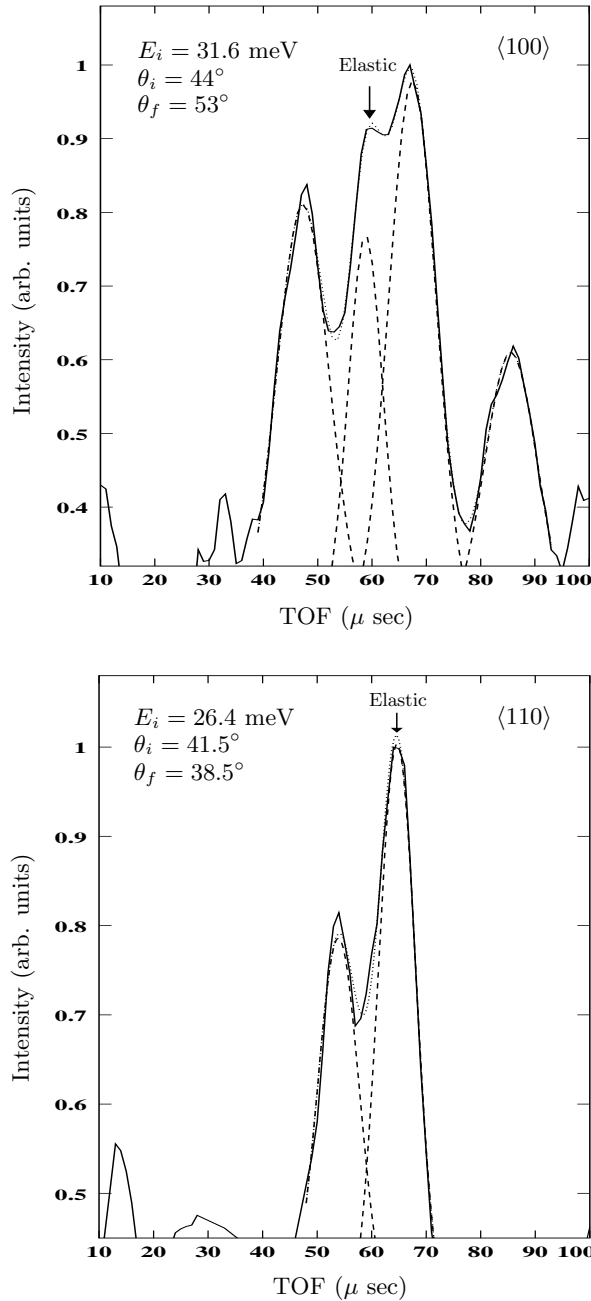


FIG. 5: Two typical TOF spectra along $\langle 100 \rangle$ and $\langle 110 \rangle$ directions (solid lines). Dashed and dotted lines are the Gaussian fits to the peaks.

namely Coulomb potential $V_{ij}^C(r) = Z_i Z_j e^2/r$ for the long-range interactions and either Born-Mayer (BM) $V_{ij}^{BM}(r) = a_{ij} e^{-b_{ij}r}$ or Buckingham $V_{ij}^B(r) = a_{ij} e^{-b_{ij}r} - c_{ij}/r^6$ potentials for the short-range interactions. Short-range interactions were limited to nearest neighbor pairs for Cu-O, O-O, Sr-O, Cl-Cl, Cu-Cl, and O-Cl, and to nearest and next nearest neighbors for Sr-Cl. Potential parameters were obtained from existing literature for Cu-O, O-O, Sr-O and Cl-Cl. Static equilibrium conditions provided four equations and were based on the methods

TABLE I: Potential parameters for pair interactions in $\text{Sr}_2\text{CuO}_2\text{Cl}_2$ and shell-model parameters.

Ions	Potential Parameters		
	<i>a</i> (eV)	<i>b</i> (\AA^{-1})	<i>c</i> (eV \AA^6)
Cu-O ^a	5814.375	4.762	0
O-O ^a	1146.25	3.279	0
Sr-O	1950	2.978 ^b	0
Cl-Cl ^c	18498.3	3.65	99.87
Sr-Cl	62037.2	4.064	0
Cu-Cl	103.55	3.0	0
O-Cl	1161.75	3.0	0

Shell-Model Parameters			.
Ion	<i>Z</i> (<i>e</i>)	<i>Y</i> (<i>e</i>)	<i>K</i> (eV/ \AA^2)
Cu	2	2.6	40
Sr	2	1.9	30
O	-2	-3.1	24
Cl	-2	-1.8	5

^aRef. 4

^bRef. 45

^cRef. 46

TABLE II: Comparison of the four measured infrared-active frequencies for $\text{Sr}_2\text{CuO}_2\text{Cl}_2$ at the center of the Brillouin zone ($q = 0$) with the values calculated by the shell model in this work. All the frequencies are in units of cm^{-1} .

Mode	Measured Frequencies		
	Ref. 41	Ref. 42	Calculated Frequencies
$E_u(1)$	525	512	522.41
$E_u(2)$	351	339	334.37
$E_u(3)$	176	173	182.67
$E_u(4)$	140	138	143.51

developed in Refs. 39 and 44.

Table I lists all potential parameters obtained either from the literature or by satisfying equilibrium conditions. These parameters were then incorporated into a shell-model to calculate the phonon dispersion curves of bulk $\text{Sr}_2\text{CuO}_2\text{Cl}_2$. In order to ensure dynamical stability over the entire BZ, $a_{\text{Cu-O}}$ was increased by %15.

The shell-model parameters, which include the ionic charge Z , the shell charge Y and the intra-ion shell-core force constant K , are also listed in Table I. These parameters were adjusted to give a best fit to the four measured^{41,42} IR-active phonon frequencies at the Γ -point. The agreement between measured and calculated frequencies is reasonably good, as can be seen in Table II, and the discrepancy between measurement and calculation is at most %5.

The eigenvectors and frequencies obtained from the shell-model for the transverse optic (TO) phonon modes of $\text{Sr}_2\text{CuO}_2\text{Cl}_2$ at $q = 0$ are depicted in Figure 6. The four E_u modes are the IR-active modes listed in Ta-

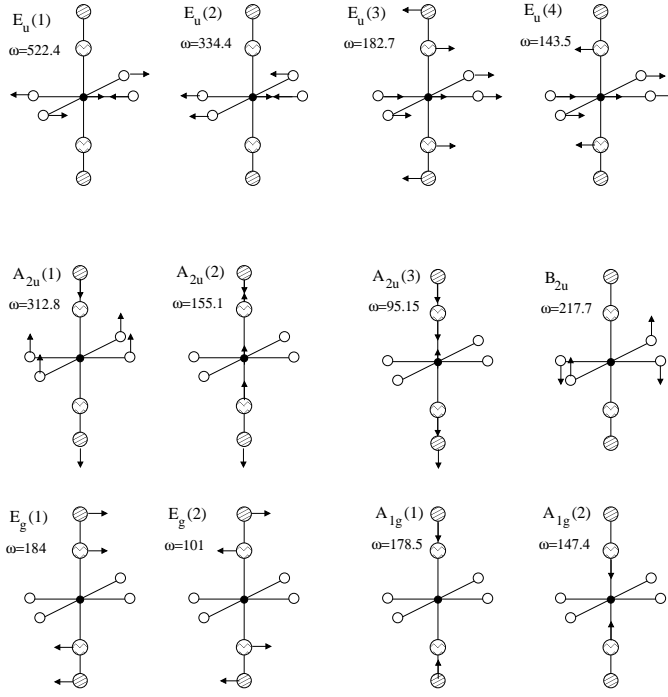


FIG. 6: The eigenvectors and frequencies of the transverse optic (TO) phonon modes of $\text{Sr}_2\text{CuO}_2\text{Cl}_2$ at $\mathbf{q} = 0$ as obtained from the shell-model. All the frequencies are in units of cm^{-1} .

ble II and are doubly degenerate. The atomic displacements corresponding to these modes are in agreement with mode assignments of Ref. 41. $E_u(1)$ is a Cu-O stretching mode, $E_u(2)$ is a Cu-O bending mode, $E_u(3)$ is the translational vibration of a Sr-atom layer against the octahedron and $E_u(4)$ is the apical bending mode of Cl against the Cu-O unit^{41,42}. The non-degenerate A_{2u} modes are also IR-active and correspond to the atomic displacements along z -direction. The doubly-degenerate E_g and non-degenerate A_{1g} modes are Raman-active and B_{2u} is silent.

The bulk BZ for body-centered tetragonal structure is shown in Figure 7 with the labelling of high-symmetry points and directions. Bulk phonon dispersion curves, calculated along Λ , Σ and ΓN directions using the shell-model of Table I, are shown in Figure 8. The longitudinal acoustic (LA) and transverse acoustic (TA) modes along all three directions are also labeled. It can be inferred from these dispersion curves that the dynamics of the $\text{Sr}_2\text{CuO}_2\text{Cl}_2$ bulk is stable throughout the BZ without any imaginary frequency.

B. Slab Lattice Dynamics

Our studies of the surface lattice dynamics of $\text{Sr}_2\text{CuO}_2\text{Cl}_2$ were also based on the shell-model. In these studies we employed slab geometries comprised of SrCl - CuO_2 - SrCl repeat unit with 21 and 33 layers and

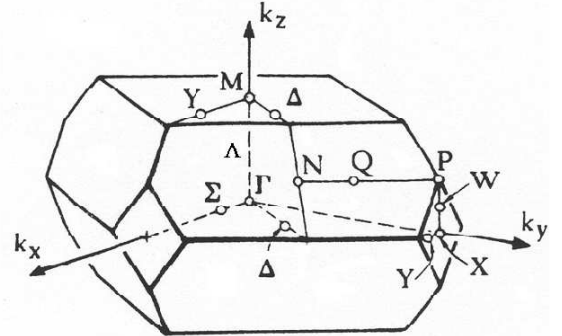


FIG. 7: The bulk BZ for body-centered tetragonal structure with the labelling of symmetry directions.

with periodic boundary conditions in the plane of the slab. The slab was bounded by two SrCl surface layers. The total number of degrees of freedom in the 33-layer slab is 231. The projection of the bulk BZ on the surface is illustrated in Figure 9. Projections of all the bulk phonon modes that lie inside the SBZ contribute to the bulk bands in slab dispersion curves.

Figure 10 shows the results of the slab calculations along both $\langle 100 \rangle$ and $\langle 110 \rangle$ directions of the SBZ where unmodified bulk shell-model parameters (Table I) were used throughout the slab. The grey areas and curves in Figures 10a and 10b are projections of the bulk modes on the SBZ (bulk bands). In Figure 10a solid black lines identify dispersion curves for shear horizontal (SH) surface phonon polarizations. These modes are polarized perpendicular to the sagittal plane (defined by the surface normal and the phonon wave vector) and parallel to the surface; they are odd with respect to reflection in the sagittal plane. Because in our scattering geometry the sagittal and scattering planes coincide and contain a high symmetry surface direction, SH modes would not be detected. In Figure 10b, solid black lines correspond to surface modes which are polarized in the sagittal plane (SP modes) and the experimental points are shown by filled squares.

From the surface dispersion curves of Figure 10 it is clear that all the SrCl surface modes are below 200 cm^{-1} . The high energy bulk bands, labeled as longitudinal optic (LO) and transverse optic (TO) bands in Figure 10a, correspond to the vibrations of Cu and O atoms in the bulk layers, consistent with the results from bulk dispersion curves.

Below 200 cm^{-1} , the agreement between the experimental points and the surface modes is reasonably good. In both directions there are experimental points which clearly fall along the surface SP modes. One example is the SP mode around 115 cm^{-1} along $\langle 100 \rangle$ (labeled by (1) in Figure 10b), which corresponds to vibration of surface Sr atom along z direction and Cl atom along x direction. Another example is the mode labeled by (2)

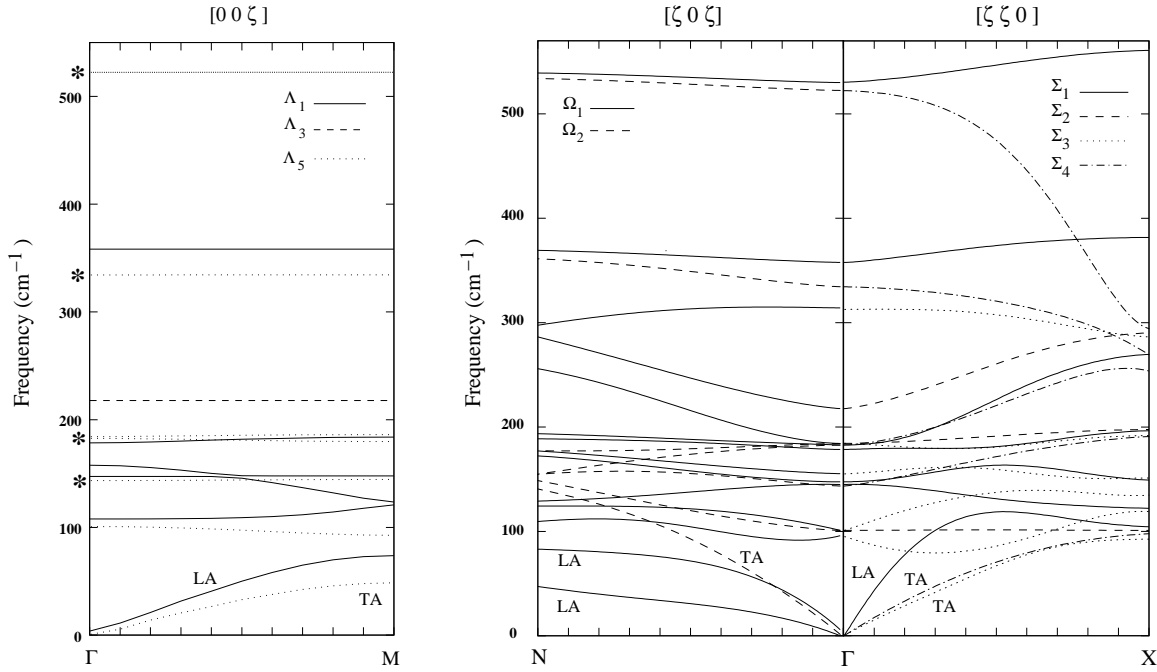


FIG. 8: Phonon dispersion curves along three symmetry directions in the bulk BZ calculated by the shell-model of Table I. The four measured^{41,42} IR-active E_u frequencies at Γ point are labeled by asterisks.

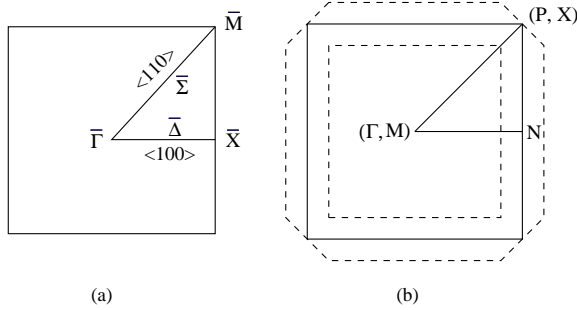


FIG. 9: (a) SBZ and (b) projection of the bulk BZ on the surface (dashed-lines).

along $\langle 100 \rangle$ direction which corresponds to the displacement of the surface Cl atom along z . Another area where there is agreement between theory and experiment is the region with a high density of bulk bands from ~ 30 to 70 cm^{-1} , close to the $\bar{\Gamma}$ point along $\langle 100 \rangle$. Because of the high density of bulk states in this region, a large number of experimental points have also been detected. Along $\langle 110 \rangle$ direction, mode (3) is associated with the vibrations of the surface Sr atom along z and mode (4) corresponds to displacements of both Sr and Cl surface atoms in the xy plane.

Along both directions, the acoustic Rayleigh modes are labeled by R. The scarcity of experimental points along the Rayleigh modes is attributed to the limitation of the energy resolution that has prevented modes with energies lower than $\sim 25 \text{ cm}^{-1}$ to be clearly identified.

Because of the systematic agreement between the SrCl surface modes and experimental dispersion points, no further adjustments of model parameters were necessary.

In order to confirm that the cleaved (001) surface of $\text{Sr}_2\text{CuO}_2\text{Cl}_2$ consists of only SrCl layers and not CuO_2 , we implemented the slab calculations for a 21-layer slab with a CuO_2 surface termination. In order to maintain the charge neutrality, the slab had to be made asymmetric, i.e. the other surface of the slab was a SrCl layer. Employing bulk shell-model parameters resulted in instabilities of several modes away from $\bar{\Gamma}$. Efforts to completely suppress these instabilities were not successful. However, we found that setting $b_{\text{Cu}-\text{O}}$ in the surface layer to 5.2 \AA^{-1} resulted in confining the instabilities to the lowest lying modes. In these calculations the optic modes of the CuO_2 surface were stable as shown in Figure 11 for SP surface modes along $\langle 100 \rangle$ direction. The instability of the lowest lying acoustic modes away from the $\bar{\Gamma}$ point is clear in Figure 11a.

By contrast to the results of slab calculation for SrCl surface, we did not find systematic agreement between the experimental data and calculated CuO_2 surface modes. For example no experimental points exist close to the surface modes labeled (1), (2) and (3) in Figure 11. Mode (1) corresponds to the vibration of O(2) surface atoms in the x direction, mode (2) corresponds to the displacements of the surface O(1) and O(2) atoms along z and mode (3) is associated with vibrations of surface Cu and O(2) atoms along z and O(1) atoms in the xz plane. The coincidental agreement of a few points with some CuO_2 surface modes (e.g. mode (4) around 125

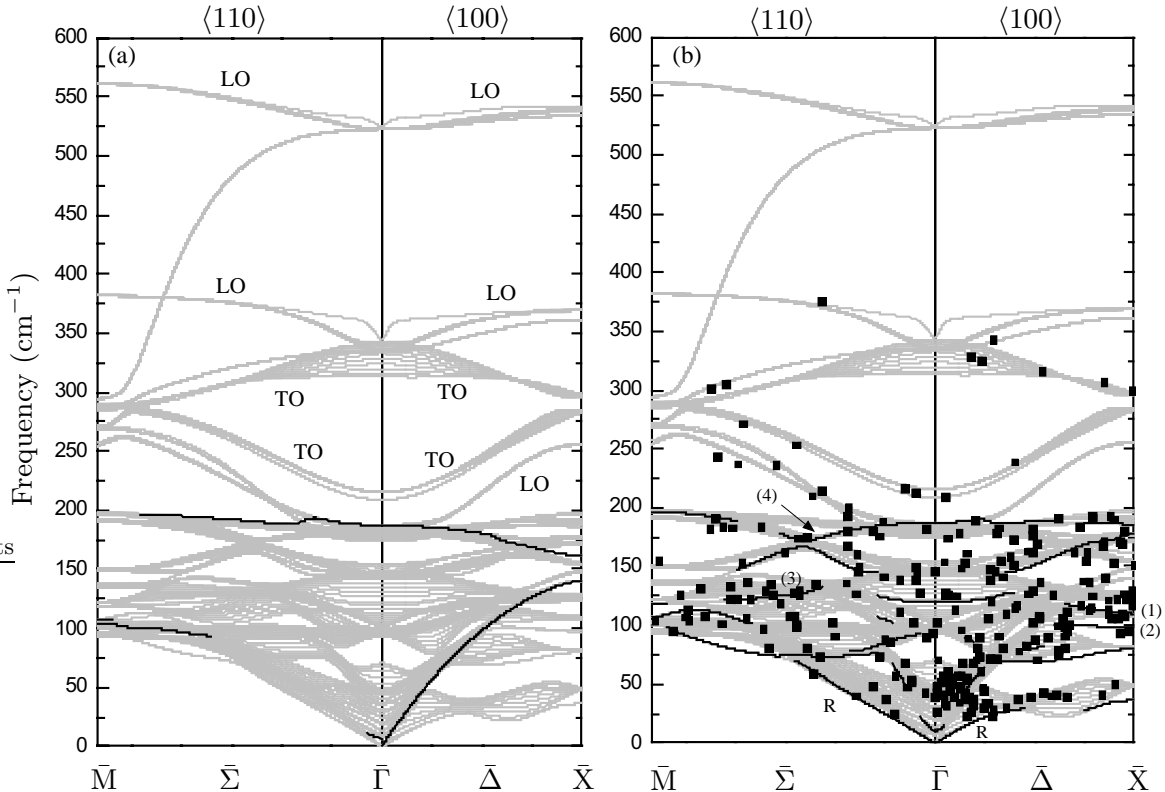


FIG. 10: Results of the slab calculation for a 33-layer slab of $\text{Sr}_2\text{CuO}_2\text{Cl}_2$ with SrCl surface termination along $\langle 100 \rangle$ and $\langle 110 \rangle$ directions. The grey curves show the bulk bands. In (a) black solid lines correspond to surface modes with SH polarization, while in (b) the black lines show SP surface modes. The filled squares are the experimental data obtained by inelastic He scattering. Modes labeled by (1), (2), (3) and (4) are discussed in the text. The acoustic Rayleigh modes are labeled by R.

cm^{-1}), is more accidental than systematic.

V. CONCLUSION

Cleaved (001) surfaces of the layered perovskite $\text{Sr}_2\text{CuO}_2\text{Cl}_2$ were prepared in UHV, and the structure and phonon dispersions of the surface were studied experimentally using elastic and inelastic HAS along high-symmetry directions of the SBZ. The position of the Bragg peaks in the diffraction patterns, obtained for different incident angles, revealed a surface periodicity consistent with bulk termination, without any evidence of surface reconstruction. This fact, along with previous LEED and x-ray photoemission results^{34,35,36} confirms that the resulting surface is non-polar and stable which favors a SrCl surface termination. A corrugation function for the SrCl surface was constructed with the aid of eikonal approximation using measured diffraction peak intensities and was in agreement with a corrugation function obtained from surface charge density calculations.

Bulk lattice dynamical calculations based on the shell-model were carried out by transferring some of the potential parameters from existing models for other cuprates like La_2CuO_4 and obtaining the rest by solving static equilibrium equations. The shell-model parameters were

adjusted to fit the four experimentally measured IR-active phonon frequencies at $\mathbf{q} = 0$. No instability were observed over the entire BZ.

Surface dynamics was investigated using slab geometry and the same shell-model. The calculations for a 33-layer slab with SrCl surfaces and a 21-layer slab with a CuO_2 surface revealed two important features. First that the experimental surface phonon dispersions obtained by inelastic HAS agreed quite reasonably and systematically with a SrCl terminated slab model. Second, the shell-model for a CuO_2 terminated slab could not be stabilized, despite all efforts. This and the fact that no experimental dispersion points lie systematically along the CuO_2 surface modes is another sign that the surface layer is SrCl and CuO_2 sheets do not exist on the surface.

Acknowledgments

The authors would like to thank J. R. Manson for helpful discussions. This work was supported by the U.S. Department of Energy under Grant No. DE-FG02-85ER45222 and in part by MRSEC Program of the National Science Foundation under award number DMR 02-13282.

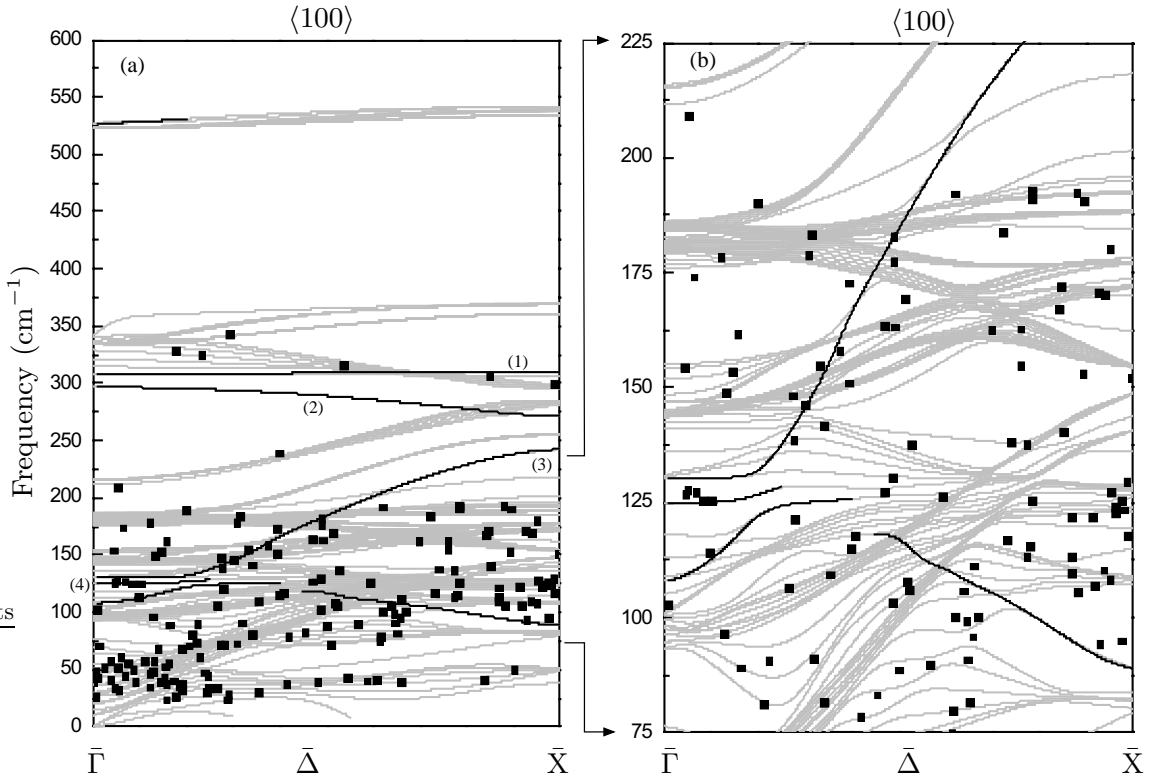


FIG. 11: Results of the slab calculation for a 21-layer slab of $\text{Sr}_2\text{CuO}_2\text{Cl}_2$ with CuO_2 surface termination along $\langle 100 \rangle$ direction. The grey curves are bulk bands, the black solid lines are the surface modes with the SP symmetry and the filled squares are the experimental data. Modes labeled by (1), (2), (3) and (4) are discussed in the text. (b) is the expansion of (a) from 75 to 225 cm^{-1} .

¹ For a review see *Surface Phonons*, Vol. 21 of *Springer Series in Surface Sciences*, edited by W. Kress and F. W. de Wette (Springer, Berlin, 1991).

² U. Paltzer *et al.*, Phys. Rev. B **54**, 11989 (1996).

³ U. Paltzer, F. W. de Wette, U. Schröder, and E. Rampf, Physica C **301**, 55 (1998).

⁴ M. Mostoller, J. Zhang, A. M. Rao, and P. C. Eklund, Phys. Rev. B **41**, 6488 (1990).

⁵ P. C. Eklund *et al.*, J. Opt. Soc. Am. B **6**, 389 (1989).

⁶ M. K. Crawford, G. Burns, and F. Holtzberg, Solid State Commun. **70**, 557 (1989).

⁷ G. Burns, G. V. Chandrashekhar, F. H. Dacol, and M. W. Shafer, Solid State Commun. **68**, 67 (1988).

⁸ W. H. Weber *et al.*, Phys. Rev. B **38**, 917 (1988).

⁹ I. Ohana *et al.*, Phys. Rev. B **39**, 2293 (1989).

¹⁰ L. Pintschovius *et al.*, Physica B **174**, 323 (1991).

¹¹ P. Böni *et al.*, Phys. Rev. B **38**, 185 (1988).

¹² R. J. Birgeneau *et al.*, Phys. Rev. Lett. **59**, 1329 (1987).

¹³ S. Hoen *et al.*, Phys. Rev. B **39**, 2269 (1989), and references therein.

¹⁴ M. K. Crawford *et al.*, Phys. Rev. B **41**, 282 (1990).

¹⁵ R. J. McQueeney *et al.*, Phys. Rev. Lett. **82**, 628 (1999).

¹⁶ L. Pintschovius and M. Braden, Phys. Rev. B **60**, R15039 (1999).

¹⁷ W. Reichardt *et al.*, Physica C: Superconductivity **162-164**, Part 1, 464 (1989).

¹⁸ A. Lanzara *et al.*, Nature **412**, 510 (2001).

¹⁹ A. W. Sandvik, D. J. Scalapino, and N. E. Bickers, Phys. Rev. B **69**, 094523 (2004), and references therein.

²⁰ L. L. Miller *et al.*, Phys. Rev. B. **41**, 1921 (1990).

²¹ M. A. Kastner, R. J. Birgeneau, G. Shirane, and Y. Endoh, Rev. Mod. Phys. **70**, 897 (1998).

²² D. Vaknin *et al.*, Phys. Rev. B. **41**, 1926 (1990).

²³ Z. Hiroi, N. Kobayashi, and M. Takano, Physica C **266**, 191 (1996).

²⁴ K. Ohishi *et al.*, arXiv:cond-mat/0412313 (2004).

²⁵ Q. Q. Liu *et al.*, Physica C **420**, 23 (2005).

²⁶ D. Vaknin, L. L. Miller, J. L. Zarestky, and D. C. Johnston, Physica C **274**, 331 (1997).

²⁷ X. L. Wang *et al.*, J. Appl. Phys. **67**, 4524 (1990).

²⁸ Y. J. Kim *et al.*, Phys. Rev. Lett. **86**, 3144 (2001).

²⁹ M. Greven *et al.*, Phys. Rev. Lett. **72**, 1096 (1994).

³⁰ T. Thio *et al.*, Phys. Rev. B **38**, 905 (1988).

³¹ T. Thio and A. Aharony, Phys. Rev. Lett. **73**, 894 (1994).

³² K. Martini, W. Franzen, and M. El-Batanouny, Rev. Sci. Instrum. **58**, 1027 (1987).

³³ P. W. Tasker, J. Phys. C: Solid State Phys. **12**, 4977 (1979).

³⁴ T. Böske *et al.*, Phys. Rev. B **56**, 3438 (1997).

³⁵ A. Koitzsch *et al.*, Phys. Rev. B. **66**, 024519 (2002).

³⁶ C. Dürr *et al.*, Phys. Rev. B **63**, 014505 (2000).

³⁷ D. Farias and K.-H. Reider, Rep. Prog. Phys. **61**, 1575 (1998), and references therein.

³⁸ F. Herman and S. Skillman, *Atomic Structure Calculations* (Prentice-Hall, Inc., 1963).

³⁹ E. Rampf *et al.*, Phys. Rev. B. **48**, 10143 (1993).

⁴⁰ S. L. Chaplot, W. Reichardt, L. Pintschovius, and N. Pyka, Phys. Rev. B **52**, 7230 (1995).

⁴¹ S. Tajima *et al.*, Phys. Rev. B. **43**, 10496 (1991).

⁴² A. Zibold *et al.*, Phys. Rev. B **53**, 11734 (1996).

⁴³ R. T. Collins, Z. Schlesinger, G. V. Chandrashekhar, and M. W. Shafer, Phys. Rev. B **39**, 2251 (1989).

⁴⁴ L. L. Boyer and J. R. Hardy, Phys. Rev. B **7**, 2886 (1973).

⁴⁵ N. N. K. nad A. V. Boris *et al.*, Phys. Rev. B **69**, 054511 (2004).

⁴⁶ G. Venkataraman, L. A. Feldkamp, and V. C. Sahni, *Dynamics of Perfect Crystals* (The MIT Press, 1975).